

Enhanced Cycling of Ni-Rich Positive Electrodes by Fluorine Modification

To cite this article: Yang Yu *et al* 2021 *J. Electrochem. Soc.* **168** 060538

View the [article online](#) for updates and enhancements.



The Electrochemical Society
Advancing solid state & electrochemical science & technology

242nd ECS Meeting

Oct 9 – 13, 2022 • Atlanta, GA, US

Abstract submission deadline: **April 8, 2022**

Connect. Engage. Champion. Empower. Accelerate.

MOVE SCIENCE FORWARD



Submit your abstract





Enhanced Cycling of Ni-Rich Positive Electrodes by Fluorine Modification

Yang Yu,¹ Yirui Zhang,² Livia Giordano,² Yun Guang Zhu,³ Filippo Maglia,⁴
Roland Jung,⁴ Forrest S. Gittleston,^{5,*} and Yang Shao-Horn^{1,2,3,**,z}

¹Department of Materials Science and Engineering, MIT, Cambridge, Massachusetts 02139, United States of America

²Department of Mechanical Engineering, MIT, Cambridge, Massachusetts 02139, United States of America

³Research Laboratory of Electronics, MIT, Cambridge, Massachusetts 02139, United States of America

⁴BMW Group, 80788 München, Germany

⁵BMW Group Technology Office USA, Mountain View, California 94043, United States of America

Ni-rich positive electrodes for Li-ion batteries can provide enhanced initial discharge capacity yet suffer from significant capacity degradation upon cycling. Fluorination of Ni-rich NMC811 positive electrodes results in a capacity retention of more than 90% after 100 cycles upon cycling to 4.4 V_{Li}. The increased cycling stability of F-modified NMC811 can be attributed to the modification of the oxide electronic structures, where density functional theory calculations shows that incorporating fluorine into the oxide lattice decrease the driving force of carbonate dissociation on the oxide surface. In situ infrared (IR) spectroscopy and ex situ X-ray photoelectron spectroscopy (XPS) further supports this argument by showing less carbonate oxidation for F-modified LiNi_{0.8}Mn_{0.1}Co_{0.1}O₂ (NMC811) than as-received NMC811 upon charging. The reduced carbonate oxidation is coupled with minimal salt decomposition on the electrode surface, as revealed by XPS. Further comparing in situ IR and XPS with that of the heat-treated NMC811 and Li₂CO₃ allows for decoupling the solvent decomposition products, where oxides are responsible for the vinylene carbonate formation with two hydrogens removed whereas surface metal carbonates promote dehydrogenated ethylene carbonate with just one hydrogen removed. This work points towards the importance of the anion engineering to increase the cycling stability of Ni-rich NMC positive electrodes.

© 2021 The Electrochemical Society ("ECS"). Published on behalf of ECS by IOP Publishing Limited. [DOI: 10.1149/1945-7111/ac0b27]

Manuscript submitted March 15, 2021; revised manuscript received May 25, 2021. Published June 23, 2021.

Supplementary material for this article is available [online](#)

LiNi_xMn_yCo_zO₂ (NMC) is widely used for the positive electrodes of Li-ion batteries, where increasing the Ni contents from LiNi_{1/3}Mn_{1/3}Co_{1/3}O₂ (NMC111) to Ni-rich NMC such as LiNi_{0.6}Mn_{0.2}Co_{0.2}O₂ (NMC 622) and LiNi_{0.8}Mn_{0.1}Co_{0.1}O₂ (NMC811) significantly increases the discharge capacity,¹⁻³ yet have a tradeoff of reduced cycling stability¹⁻⁵ and thermal stability,^{3,6,7} with lower onset potentials of CO₂ and O₂ formation.^{1,2,8} The reduced cycling stability comes from the surface electronic structures of the oxides.^{9,10} Previous computational^{9,11} and experimental studies^{10,12} have shown that the dissociation of carbonate electrolyte solvent in electrolyte becomes more favorable on NMC with increasing Ni content (increased M-O covalency), forming surface hydroxyl group (e.g. C₃O₃H₃⁺-O_{surface} and H⁺-O_{surface}), and reducing surface transition metals.⁹⁻¹² The surface hydroxyls group can further attack the LiPF₆ salt, generating decomposed salt species such as Li_xPF_yO_z and PF₃O probed by ex situ fourier transformed infrared spectroscopy (FT-IR) as well as X-ray photoelectron spectroscopy (XPS). The decomposed species deposited on the surface contribute to the impedance growth on the electrode surface, rationalizing the decreased cycling performance observed experimentally for Ni-rich NMC^{1,4,5} compared to NMC111¹ and LiCoO₂.¹³ Recent density functional theory (DFT) screening work by Giordano et al.⁹ has shown that the compounds with ligand *p*-band further away from the Fermi level such as Al₂O₃ and NiF₂, demonstrated much lower driving force for carbonate oxidative dehydrogenation. Such trend is in agreement with ex situ¹⁴ and in situ¹² FT-IR work on Al₂O₃-coated NMC622 has demonstrated much less carbonate decomposition as well as salt decomposition, in comparison to uncoated NMC622. Moreover, such suppressed solvent and salt decomposition are shown to be coupled with enhanced cycling stability of the Al₂O₃-coated NMC622¹⁵⁻¹⁸ with less internal resistance build-up, compared to uncoated oxides.¹⁵⁻¹⁸ Further support comes from recent works of Janek and coworkers¹⁹ as well as Xiong et al.,²⁰ where 1%–4% fluorine

doping of NMC811, using PvDF as a fluorinating agent, results in more stable cycling yet smaller discharge capacity compared to those of pristine NMC811 upon charging to 4.2 V_{graphite} with 0.5 C rate (~14 mA g⁻¹). This enhanced cycling performance of F-doped NMC811 is in contrast with less stable cycling of N-doped NMC81, rooted in difference in the surface electronic structures of F- and N-doped oxides, where F has a larger electronegativity compared to O and N, resulting in lower ligand *p*-band and less surface reactivity and more stable interface. Unfortunately, the detailed interface reaction between the F-modified electrode and carbonate-based electrolyte is not well understood, while those previous works mainly focus on the evolution of oxide structures upon cycling, probed by X-ray diffractometry (XRD) as well as scanning electron microscopy (SEM). More recently, Gasteiger et al.²¹ have shown that heat-treated NMC811 to remove surface impurity phases such as carbonates results in enhanced cycling stability, which arises questions to the role of surface F modification on reducing electrolyte oxidation and increase cycling stability as the surface modification processes involve heat-treatment at the temperatures high enough to remove surface impurity phases. Moreover, the root cause for the improved cycling stability of F-modified NMC is also not clearly pointed out, inhibiting further optimization of anionic substitution strategies to improve the cycling performance of Ni-rich NMC positive electrodes.

In this work, we have used a one-pot solid-state synthesis of F-modified NMC811, which shows increased cycling stability in comparison to pristine NMC811. By employing in situ FT-IR, coupled with XPS, we probe a much more suppressed signal coming from vinylene carbonates and dehydrogenated EC from C=O region in FT-IR and C1s and O1s spectra in XPS, typical parasitic products from carbonate decomposition. Furthermore, comparing the F-modified NMC811 with the heat-treated and as-received NMC811, we are able to decouple the impact of fluorine surface modification in NMC from that of Li₂CO₃-like surface contaminants on the cycling performance, highlighting the importance of surface electronic structure engineering of oxides materials on the cycling performance of positive electrodes and Li-ion batteries.-

*Electrochemical Society Member.

**Electrochemical Society Fellow.

^zE-mail: shaohorn@mit.edu

Result and Discussion

Fluorine substitution lowers the ligand p -band and dehydrogenation driving force.—DFT calculations shows substituting oxygen with fluorine in LiNiO_2 lower the overall ligand p band with respect to the Fermi level, correlated with reduced carbonate dehydrogenation driving force for fluorine substituted LiNiO_2 in comparison with LiNiO_2 . By replacing half of the oxygen anion in the bulk LiNiO_2 , the ligand p band center downward shifts away from the Fermi level in comparison with the pristine LiNiO_2 , as shown in Figs. 1a and 1b. This ligand p -band downward shifts comes from a more electronegative ligand fluorine as well as Ni reduction by substituting O^{2-} to F^- , resulting in higher energy barrier for electron transfer from the electrolyte. (Fig. 1a) Such downward shift of bulk ligand p -band corresponds to an upward shift of the Fermi level on the absolute energy scale, potentially resulting in higher energy penalty of hydrogen adsorption based on the trend established in our previous work,⁹ which is scaled with energy penalty for carbonate oxidative dehydrogenation.^{11,22} (Fig. 1b) By substituting 12.5% F^- on the $(10\bar{1}4)$ surface of LiNiO_2 to lower the surface ligand p -band, there is a 0.5 eV decrease of the carbonate dehydrogenation driving force on the oxide surface, inducing more stable oxide-electrolyte interface. (Fig. S1 (available online at stacks.iop.org/JES/168/060538/mmedia))

We used a one-pot solid-state synthesis to experimentally incorporate F into the NMC811 lattice at 600 °C, where we used NH_4F as the fluorinating agent as well as LiOH to compensate for the lithium loss during the fluorination. (Detailed procedures outlined in Methods section) Energy dispersive X-ray analysis (EDX) showed largely uniform distribution of fluorine ions within and across particles with some concentrated spots for fluorine, signaling the formation of metal fluorides on the particle surface (Fig. 2a). However, due to the detection limit of EDX measurement (typically above 5%), we could not obtain a reliable estimation of the overall F-contents for F-modified NMC811 from EDX. The average incorporation of fluorine into the surface is around 4%–5%, from XPS high-energy resolution survey (Supplementary Information Table 1), matching with the initial concentration of fluorinating agent introduced during synthesis. The majority of the fluorine is concentrated on the surface, where the fluorine contents dropped

significantly after around 20 min of Ar^+ sputtering (corresponding to around 5 nm depth) with voltage 1 kV and current 1 μA (Fig. S2). However, we did not quantify the composition for the composite electrodes due to the overwhelming surface area effect coming from the conducting carbon and binder, which might interfere with the quantification of atomic percentage. Moreover, we should note that the quantification of XPS is the relative atomic percentage on the surface and highly dependent on the instrument as well as the penetration depth, therefore it might not be the most accurate quantification of the fluorine contents. To more accurately capture the depth-dependent information of the fluorine distribution, future characterization using EDX as well as the electron energy loss spectrum on the cross-section of the active materials is needed. Further optimization of the synthesis route with longer mixing time could be achieved in future studies to achieve a better homogeneity in the particle. Moreover, upon heat treatment to 600 °C under oxygen, there is also an obvious removal of surface carbonyl group from the as-received NMC811, shown by XPS C1s of the as-received and F-modified NMC811 (Fig. 2b). Upon fluorination at 600 °C, there is a decrease of high-binding energy feature, marking the removal of surface carbonate and carbonyl group ($\text{O}-\text{C}=\text{O}$) during the heat-treatment. F1s XPS spectra of F-modified NMC811 shows successful incorporation of fluorine on the oxides, showing major contribution of metal (oxy-)fluorides in comparison with as-received NMC811.

In situ IR shows evidence of diminished solvent decomposition on charged F-modified NMC.—In situ IR shows that charged F-modified NMC811 exhibits less electrolyte solvent dehydrogenation upon charging to 4.8 V_{Li} , in comparison to pristine NMC811 as well as heat-treated NMC811. Attenuated total reflectance (ATR) spectra is composed of three major peaks in the $\text{C}=\text{O}$ region of pristine LP57 electrolyte (1 M LiPF_6 in ethylene carbonate (EC):ethyl methyl carbonate (EMC) solution) (Fig. 3), located at around ~ 1807 , ~ 1773 , and $\sim 1744 \text{ cm}^{-1}$, which can be attributed to $\text{C}=\text{O}$ stretching of EC molecule, Li^+ -coordinated EC molecule, and EMC molecule, respectively. This assignment is based on the comparison of the ATR spectra of EC, EMC and 1 M LiPF_6 in EMC solution from our previous work.^{10,12} Upon charging the as-received NMC811 particle up to 3.8 V_{Li} and above, there is an obvious

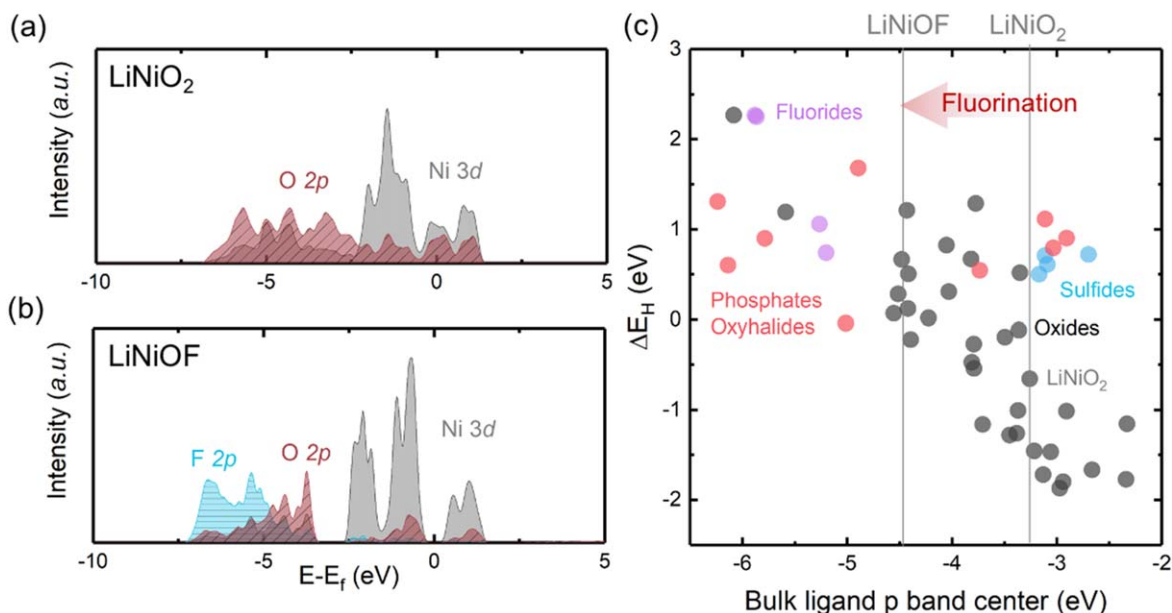


Figure 1. (a) Projected density of states (pDOS) of LiNiO_2 (top panel) and substituted LiNiOF (bottom panel), where by fluorine substitution there is an obvious reduction of the Ni by substituting O^{2-} with F^- , which also shifts the ligand band center downwards due to the larger electronegativity of F compared to O. The Ni 3d, O 2p and F 2p density of states are represented by grey, red and blue shades, respectively. (b) Hydrogen adsorption energy on the materials surface plotted against bulk ligand p band center (eV), where from the trend we established with other materials in previous work,⁹ by fluorination, we are able to push down the ligand p -band, decrease the hydrogen adsorption energy and carbonate dissociation driving force.

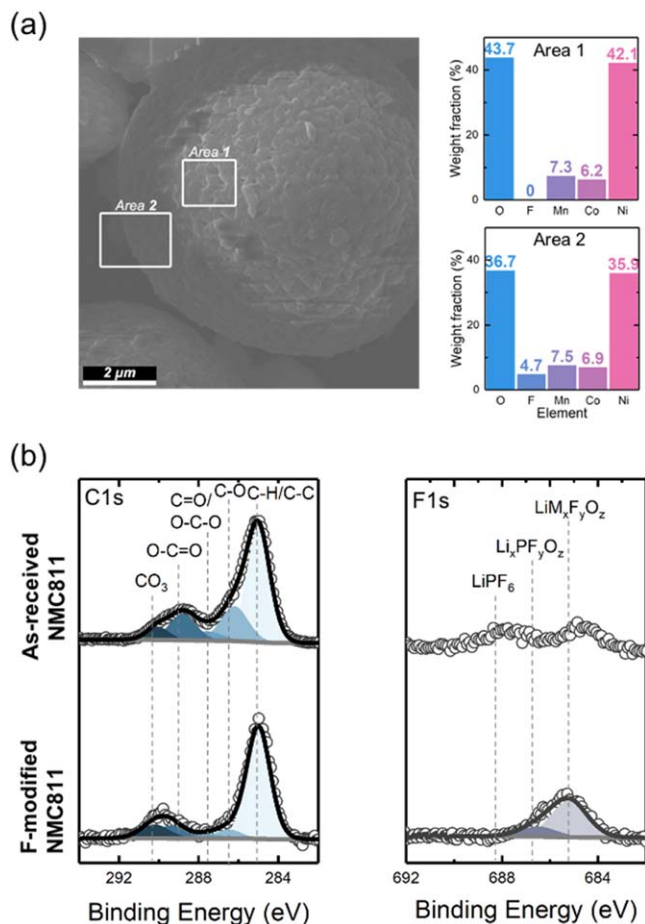


Figure 2. (a) SEM image of the F-modified NMC811, where EDX information is taken in Area 1 and Area 2, where we do see a slight non-uniformity of the fluorine distribution on the particle while the secondary particle integrity is maintained. (b) C1s and F1s XPS spectra of as-received NMC811 and F-modified NMC811 (with 5% nominal stoichiometric F), where upon the heat-treatment, there is a removal of surface carbonate and carbonyl group, accompanied by surface fluorination. The XPS data of as-received NMC811 is from our previous work.¹⁰

growth of a convoluted feature in 1800 cm⁻¹ to 1830 cm⁻¹ wavenumber in the difference IR spectra (Fig. 3b). This convoluted feature is composed of peaks at 1830 cm⁻¹,^{10,12} 1820 cm⁻¹,^{10,12} 1813 cm⁻¹,^{10,12} which corresponds to C=O stretching of vinylene carbonate (VC), EC-based oligomers, dehydrogenated EC, respectively.^{10,12} The growth of those EC-derivative species comes from the dehydrogenation of EC molecules on the oxide surface, forming dehydrogenated EC. The dehydrogenated EC adsorbed on the surface could continue form EC-based oligomeric species with other chain carbonate-derived species in the electrolyte.^{10,11} Moreover, the formation of VC species could come from removing two hydrogen atoms from the EC molecules through oxide mediation and/or attack of singlet oxygen from the electrolyte.^{10,23,24} Those decomposition products signal the intense interfacial reactions between as-received NMC811 and conventional carbonate electrolyte. In comparison, the difference IR spectra of F-modified NMC811 (Fig. 3a) shows minimum changes upon charging up to 4.8 V_{Li}. The minimal spectra changes suggest minimal surface reactivity of F-modified NMC811 towards electrolyte, which is maintained after 3 cycles (Fig. S3). This observation indicates stable oxide surfaces upon cycling towards carbonate dissociative adsorption (C₃O₃H₄ + 2 O-M³⁺-O → *C₃O₃H₃⁺ + *H⁺ + 2 O-M²⁺-O).^{10,11} This in situ FT-IR spectra of F-modified NMC811 is comparable to that of NMC111 measured in previous work,¹² showing negligible interface reactivity upon three cycles, much less reactive compared

to as-received NMC622 and 811.¹² It is worthy to note that the lack of decomposed species observed for F-modified NMC811 in the IR spectra only indicates a more diminished interfacial reactivity compared to as-received NMC811 at the same scale rather than complete absence of interfacial reactions. The observed suppressed electrolyte decomposition for F-modified NMC811 presented in this work is also in agreement with improved capacity retention of F-doped NMC811 upon charging to 4.3–4.4 V_{Li} shown by Janek et al.,¹⁹ Xiong et al.,²⁰ as well as Breddemann et al.²⁵ through solid-state, sol-gel and gas-flow reactor synthesis.

By contrasting to heated-treated NMC 811, we showed that the reduced electrolyte oxidation of F-modified NMC811 does not solely come from the effect from heat-treatment. By heat-treating the NMC811 at 600 °C without any fluorine source and Li compensation, heat-treated NMC811 were found to be free of carbonate contaminants as blank sample for comparison as shown by the XPS C1s data. (Fig. 4c). Heat-treated NMC811 shows noticeable increase in the overpotential compared to pristine NMC811 as well as fluorine-modified NMC811 (Fig. 3c), indicative of Li-deficient phases formed on the oxide surface due to the heat treatment. Upon charging the heat-treated NMC811 up to 4.0 V_{Li} and above, in situ IR spectra (Fig. 3c) revealed growing signal at ~1830 cm⁻¹, indicative of VC formation but without dehydrogenated EC and EC-based oligomeric species located at ~1813 cm⁻¹, 1820 cm⁻¹, respectively. This species could not come from the EMC-derived species, as C=O stretching mode in linear carbonate usually located around and below 1750 cm⁻¹,¹⁰ as demonstrated in our previous work.¹⁰ This observation suggests innate NMC811 oxide surface without Li₂CO₃ contaminants, specifically the oxygen sites, promotes the formation VC, generated from EC by removing two hydrogen atoms and forming a C=C double bond. (C₃O₃H₄ + 2 O-M³⁺-O → *C₃O₃H₂ + 2 *H⁺ + 2 O-M²⁺-O)²³

On the other hand, we propose that surface carbonate Li₂CO₃ present on as-received NMC811, without heat-treatment, promotes the formation of deH-EC and EC-derived oligomers. This hypothesis is supported by in situ IR spectra of composite Li₂CO₃ electrodes undergoing a linear voltage sweep. Upon charging Li₂CO₃ to 3.9 V_{Li}, significant decomposition current up to 20 μA was found, which was accompanied with increased signal ~1813 cm⁻¹, signaling the growth of dehydrogenated EC^{10,12} and oligomeric species^{10,12} on the surface of Li₂CO₃ (Fig. 3d). The decomposition current of Li₂CO₃ was accompanied with the conversion of Li₂CO₃ into CO₂, evidenced by the differential electrochemistry mass spectrometry (DEMS) of Li₂CO₃. Upon charging Li₂CO₃ composite electrode to 3.9 V_{Li} and above, CO₂ evolution was accompanied with minimum oxygen evolution (Fig. S15), and the rate of CO₂ evolution was roughly half of the electron transfer calculated by the coulomb counting from the decomposition current. There are generally two schools of thoughts in how Li₂CO₃ decompose upon charging to 3.9 V_{Li} and above. The first school of thoughts propose that upon charging, Li₂CO₃ decomposition follows the electrochemical pathway^{36–39}: 2Li₂CO₃ → 4e⁻ + 4Li⁺ + 2CO₂ + O₂, which evolves CO₂ and 0.5 O₂ per 2e⁻ transferred. This previous work claimed the oxygen evolved from the electrochemical decomposition is the highly reactive singlet oxygen, shown by singlet oxygen trap 9,10-dimethylanthracene (DMA).³⁷ Such singlet oxygen is shown in previous studies to attack the carbonate electrolyte and form CO₂.²³ Therefore the singlet oxygen usually could not be captured by the DEMS measurement.^{23,24} However, in the DEMS measurements presented in this and previous work, there is only one CO₂ evolved per 2e⁻ transferred without additional O₂ and CO₂ evolution observed, supposedly coming from the singlet oxygen. Moreover, the singlet oxygen trap DMA used in this study³⁷ oxidizes electrochemically (C₆H₁₄ → C₆H₁₃⁺ + e⁻) upon charging to 3.9 V_{Li} and above (Fig. S16), and therefore cannot be a reliable singlet oxygen indicator at 3.9 V_{Li} and above, which weakens the support for the school of thoughts.³⁷ Another school of thoughts propose that carbonates chemically decompose through an acid-base reaction.²¹ 4H⁺ + 2Li₂CO₃ → 4Li⁺ + 2CO₂ + 2H₂O, where such

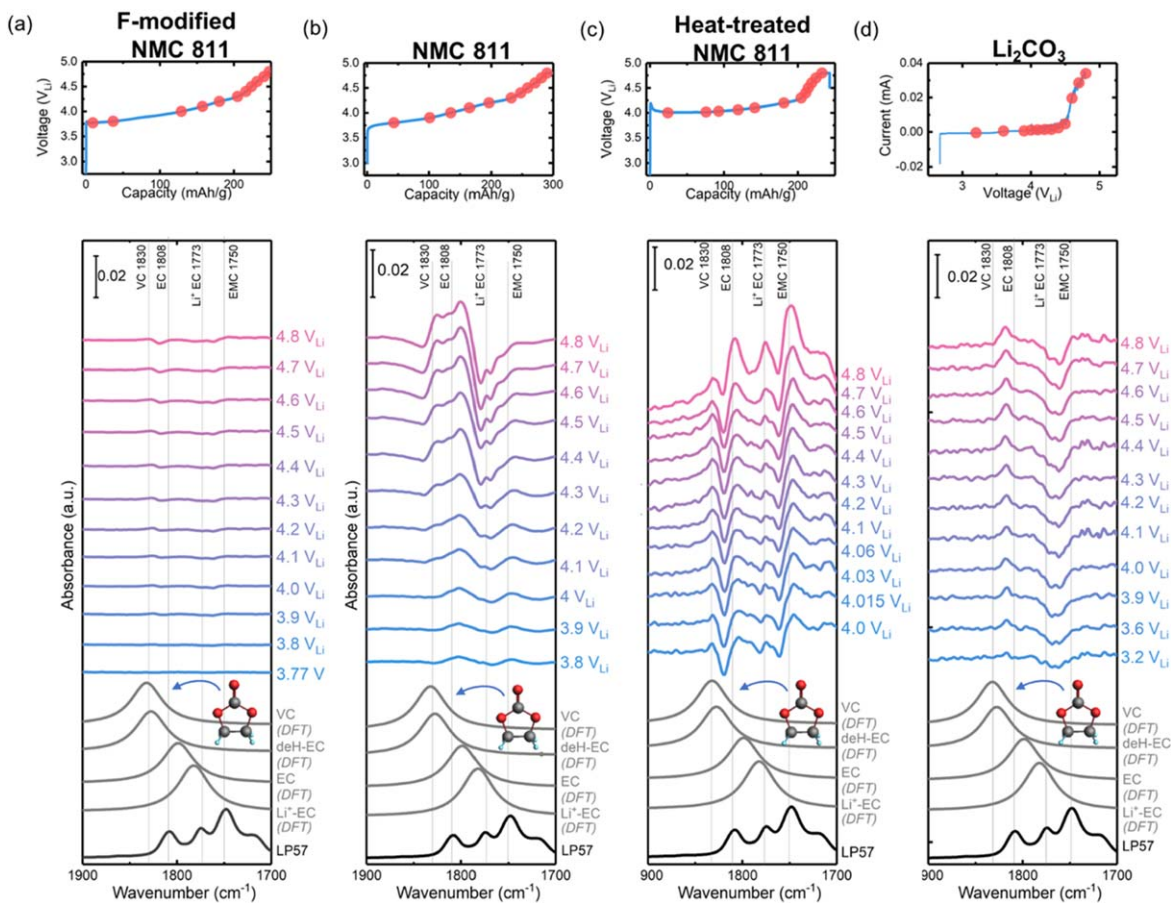


Figure 3. In situ difference FT-IR spectra of composite (a) F-modified NMC811 (with 5% nominal stoichiometric F), (b) as-received NMC811,¹² and (c) heated-treated NMC811, upon lithium deintercalation and charged to 4.8 V_{Li}, with a current rate of 28 mA g⁻¹ (C/10). (d) In situ FT-IR spectra of composite Li₂CO₃ undergoing a linear voltage sweep with a scan rate of 0.12 mV sec⁻¹. Upon charging, as-received NMC811 shows significant decomposition starting from 4 V_{Li} of ethylene carbonate decomposition including vinylene carbonate (VC), EC-based oligomers, dehydrogenated EC located at around 1830 cm⁻¹, 1820 cm⁻¹, 1813 cm⁻¹. In contrast, F-modified NMC811 shows absence of the decomposition of carbonate when compared in the same scale. For the heat-treated NMC811 sample, there is only a signature of VC formation at 1830 cm⁻¹ starting from 4 V_{Li}, whereas for Li₂CO₃ composite electrodes, there is only obvious signal of dehydrogenated EC at 3.9 V_{Li} and above.

decomposition only has CO₂ release without any O₂ release, matching with previous DEMS measurement on the absence of O₂ signal upon charging Li₂CO₃.^{21,37} the protons could either come from protic species in the pristine electrolyte²¹ or from the dehydrogenation of electrolyte solvent at high potentials, supported by in situ IR (Fig. 3d). Therefore, we believe that the surface Li₂CO₃ decomposes in the form of acid-base reaction with the protons provided by carbonate electrolyte decomposition accompanied with the formation of oligomeric species, as observed by in situ IR measurement (Fig. 3d).

Ex situ XPS shows evidence of reduced solvent and salt decomposition on charged F-modified NMC.—Further support for reduced electrolyte decomposition of F-modified NMC811 came from ex situ XPS C1s and O1s of the charged F-modified NMC811 as shown in Figs. 4a and 4d, which were collected from oxide-only electrodes charged to discrete voltages at rate of 2.8 mA g⁻¹ (C/100), followed by 5 h potential holding. The C1s spectra (Fig. 4a) were fitted to components including adventitious carbon or C-H bonds (285.0 eV),^{26,27} C-O²⁸ bonds in ROLi (286.3 eV),³¹ polyethers or R-CH₂-OCO₂Li species (287.6),^{34,40} C=O/O-C-O bonds (288.8 eV)^{28,29} like in acetals, and O=C-O²⁸ as in esters or carboxylates,³¹ respectively. Charging the F-modified NMC811 to 4.6 V_{Li} resulted in negligible changes in the C1s spectra, which is in contrast to significant changes observed to C-O bonding from the oligomeric species from electrolyte decomposition upon charging as-received NMC811 (Fig. 4b) as reported previously.¹⁰ The

enhanced stability of charged F-modified NMC811 to as-received NMC811 is further supported by O1s XPS spectra upon charging to 4.6 V_{Li}, (Fig. 4d) where minimum changes were noted in the intensity of lattice oxygen peak at ~529 eV as well as ~533.4 eV for the O=C=O bond in esters. In contrast, charging as-received NMC811 to 4.2 V_{Li} and above, there was a significant increase in the C-O component in the C1s (Fig. 4e), coupled with significant reduction in lattice oxygen peak in O1s (Fig. 4a), which is in agreement with previous work.¹⁰ This observation can be attributed to the formation of oligomers such as EC-based and VC-based oligomer coming from oxidative dehydrogenation of EC and EMC solvent, later deposited on the oxygen lattice.^{1,2}

Reduced solvent oxidation of F-modified NMC811 is accompanied with reduced salt decomposition, revealed by ex situ XPS F1s spectra, shown in Figs. 5a, 5d, and Fig. 6a. F1s of pristine F-modified NMC surface shows predominantly the contribution of metal (oxy-)fluorides at around 685 eV,³¹ indicative of no obvious surface residual of reaction precursors. While charging F-modified NMC811 to 4.1 V_{Li} was accompanied with growing signal at around 686.5 eV as well as 687 eV.³¹ (Fig. 5d) Further charging up to 4.6 V_{Li} resulted in no significant changes in the relative intensities of these features. These components can be assigned to metal (oxy-)fluorides (LiM_xF_yO_z) at 685 eV³¹ from, lithiated fluorophosphates (Li_xPF_yO_z) at ~686.5 eV³¹ for, as well as the residual electrolyte salt LiPF₆ for ~687 eV.³¹ Therefore, charging from the pristine state to 4.1 V_{Li} predominantly results in a slight attachment of electrolyte salt LiPF₆ on the electrode surface at around 687 eV, and salt

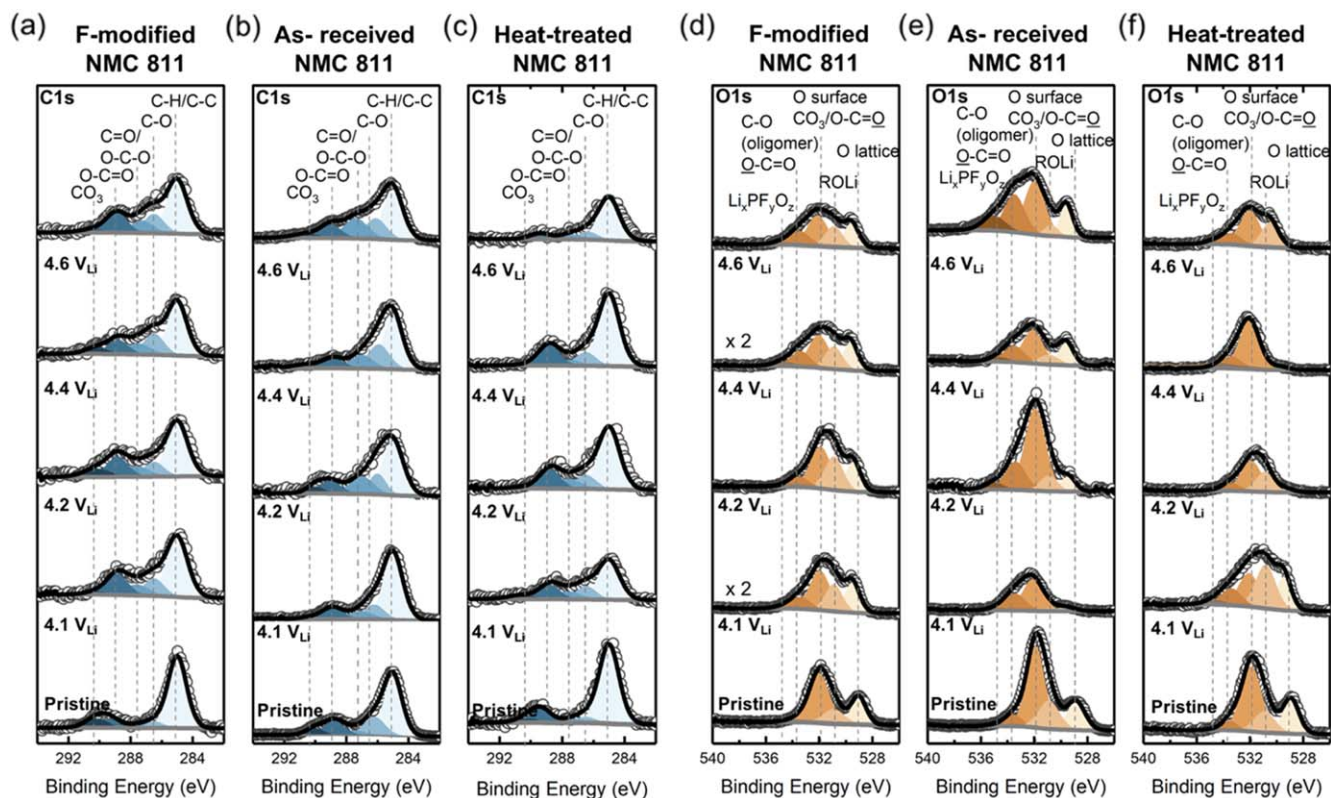


Figure 4. Ex situ XPS spectra C1s of pristine and charged (a) F-modified NMC811, (b) as-received NMC811,¹⁰ and (c) heat-treated NMC811, O1s of pristine and charged (d) F-modified NMC811, (e) as-received NMC811, and (f) heat-treated NMC811 oxide-only electrodes, where the electrodes are charged to 4.1, 4.2, 4.4 and 4.6 V_{Li} . By comparing. All spectra were calibrated with the adventitious hydrocarbons at 285.0 eV and background corrected using a Shirley background. C1s spectra were assigned with the following contributions: C-H/C-C (~ 285 eV),^{26,27} C-O (~ 286.3 eV),²⁸ C=O/O-C-O (~ 287.6 eV),^{28,29} O=C-O (~ 288.8 eV)²⁸ and CO_3 (~ 290.3 eV).³⁰ O1s spectra were assigned with the following contributions: O lattice (~ 529.3 eV),³¹ ROLi (~ 531 eV),³² surface O/CO₃/O-C=O (~ 532 eV),^{30,33} C-O/O-C=O/OP(OR)₃ ($E_b \sim 533.4$ eV)^{29,31,34} and $Li_xPF_yO_z$ ($E_b \sim 534.8$ eV).³⁵ The P2p spectra are shown in Fig. S4. The reproducibility data are shown in Figs. S5–S14. The deconvolution parameters are shown in Tables S1 and S2.

decomposition products such as lithiated fluorophosphates ($Li_xPF_yO_z$) at ~ 686.5 eV, accompanied with no significant intensity change in the metal oxyfluorides on the native oxides. Further charging up to 4.6 V_{Li} does not result in significant changes in the components of lithiated fluorophosphates (686.5 eV), metal (oxy-) fluorides (685 eV) and the residual salt (687 eV) on the oxide surface, indicative of very stable fluorides layer and halted salt decomposition at high state-of-charge for the oxides. The stable fluoride layer on F-modified NMC811 at high state-of-charge was further confirmed with lack of obvious shift observed in N2p XPS spectra with increasing voltage (Fig. 5f) and minimum changes in the peak relative intensity in P2p XPS spectra. (Fig. S9)) Pristine F-modified NMC811 has a Ni2p peak around 854.4 eV, in comparison with 854.5 eV for pristine nonmodified NMC811, representing the existence of nickel (oxy-)fluorides on the surface introduced by the synthesis.¹⁰ Further charging of F-modified NMC811 reveals no shift in Ni2p main peak, suggesting stable nickel (oxy-)fluoride layers charged to 4.6 V_{Li} . This observation is in line with minimum changes in the relative intensity of the phosphates, metal (oxy-) fluorophosphates and PF_6 components in the P2p XPS spectra (Fig. S9) spectra in F-modified NMC811 charged to 4.6 V_{Li} .

In contrast to the reduced salt decomposition and stable fluoride layers observed in F-modified NMC811, charged as-received NMC811 (Figs. 5b and 5e) shows drastic electrolyte salt decomposition and strong surface reactivity as a function of potential as shown in our previous work.¹⁰ Upon charging the as-received NMC811 to 4.2 V_{Li} , there is significant growth of components at ~ 685 eV and ~ 686.5 eV as reported previously,¹⁰ representing salt decomposition into metal (oxy-)fluorides³¹ and fluorophosphates.³¹ Further charging up to 4.6 V_{Li} results in significant decrease of

components ~ 685 eV and ~ 686.5 eV, marking the decomposition of metal (oxy-)fluorides and fluorophosphates at high state-of-charge, potentially attributed to further decomposition of $Li_xPF_yO_z$ into gaseous products such as PF_3O .⁴² This observation indicates unstable salt-derived layers in charged as-received NMC811. Ni2p spectra of charged as-received NMC811 further supported the observation of unstable electrolyte salt-derived layers on the oxide surface. Upon charging to 4.2 V_{Li} , a positive shift of the Ni2p main peak by 2 eV from 854.5 eV to 857–588 eV was observed, representing salt decomposition forming nickel oxyfluorides on oxide surface.¹⁰ Further charging to 4.6 V_{Li} is followed by a backshift of Ni2p spectra, indicative of the unstable salt-derived layers at high state-of-charge. (Fig. 5e)

XPS C1s and F1s spectra of the heat-treated NMC811 and Li_2CO_3 further supports that the reduced solvent and salt decomposition of F-modified NMC811 do not solely come from the removal of surface impurities from heat-treatment. Charged heat-treated NMC811 to 4.6 V_{Li} does not show a significant growth of C-O component at 286.3 eV in the XPS C1s spectra (Fig. 5c), indicative of lack of formation of oligomeric species and dehydrogenated EC, matching with the lack of 1813 cm^{-1} and 1817 cm^{-1} spectroscopic features in charged heat-treated NMC811 in Fig. 3c. In contrast, XPS C1s spectra of charged Li_2CO_3 showed the growth of C-O component upon charging to 4.0 V_{Li} and above, (Figs. S17a and 6d) suggesting the formation of EC-based oligomers, coming from dehydrogenated EC. This observation further confirms that surface contaminants such as carbonates are responsible for the formation of deH-EC and EC oligomers, while metal oxides are responsible for the VC formation, supported by in situ IR spectra of charged heat-treated NMC811 (Fig. 3c). Both VC and deH-EC formation generate

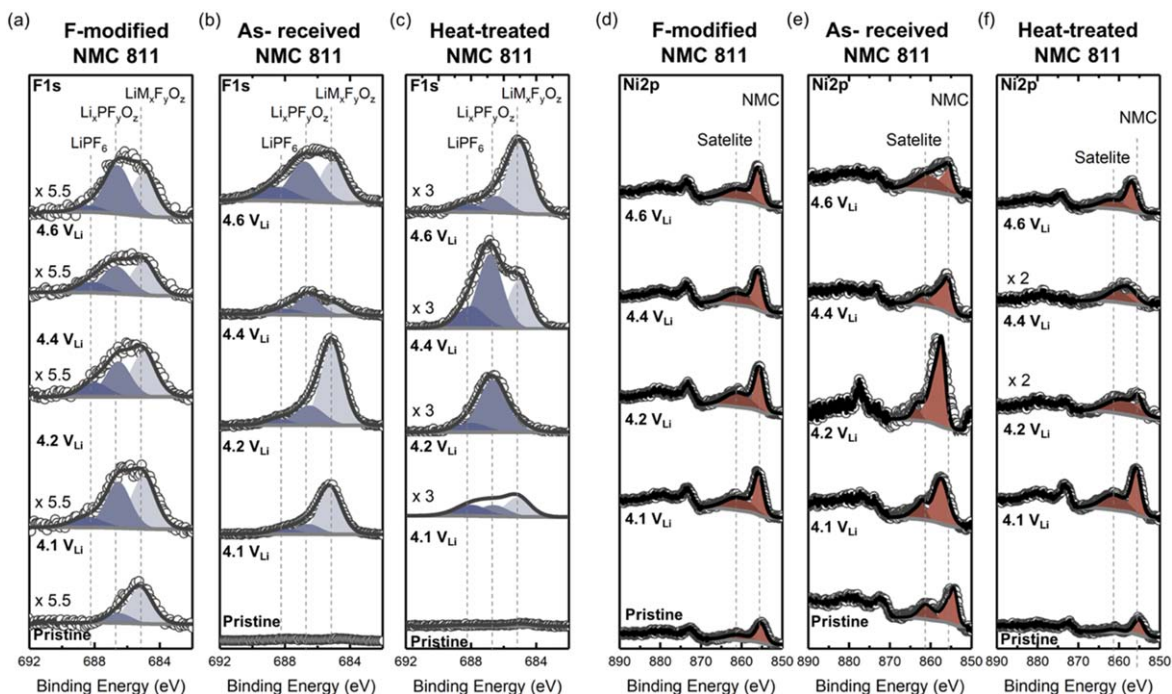


Figure 5. Ex situ XPS spectra F1s of pristine and charged (a) F-modified NMC811, (b) as-received NMC811,¹⁰ and (c) heat-treated NMC811, Ni2p of pristine and charged (d) F-modified NMC811, (e) as-received NMC811, and (f) heat-treated NMC811 oxide-only electrodes, where the electrodes are charged to 4.1, 4.2, 4.4 and 4.6 V_{Li}. All spectra were calibrated with the adventitious hydrocarbons at 285.0 eV and background corrected using a Shirley background. The F1s spectra were deconvoluted to three different species: lithium or metal fluoride species around 685 eV,³¹ lithium or metal fluorophosphate around 686.5 eV and lithium hexafluorophosphate around 688 eV.⁴¹ The P2p spectra are shown in Fig. S4. The reproducibility data are shown in Figs. S5–S14. The deconvolution parameters are shown in Table S1 and S2.

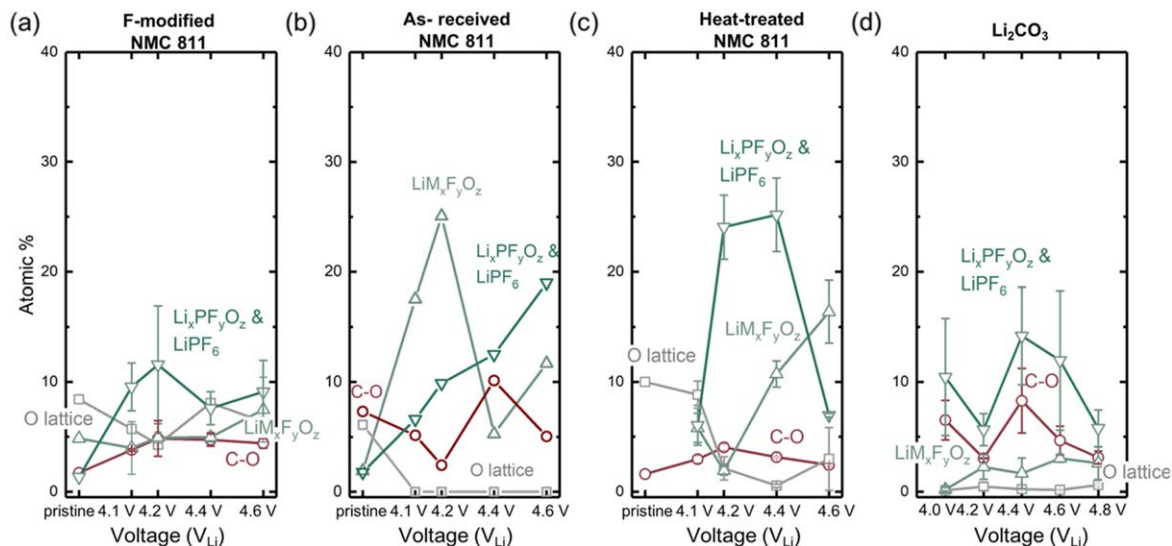


Figure 6. XPS Atomic percentage quantification of different surface species of pristine and charged (a) F-modified NMC811, (b) as-received NMC811,¹⁰ and (c) heat-treated NMC811 oxide-only electrodes, where the electrodes are charged to 4.1, 4.2, 4.4 and 4.6 V_{Li}. (d) Atomic percentage quantification of different surface species of charged Li₂CO₃ to 4.0, 4.2, 4.4, 4.6, and 4.8 V_{Li}. The quantification was performed by fitting the raw XPS spectra in Figs. 3 and 4, where the atomic percentage and corresponding error bar are obtained by averaging the quantification results obtained from two samples charged to the same potential as shown in Figs. S5–S14 and Figs. S18–S20. The deconvolution parameters are shown in Tables S1–S3.

surface hydroxyl group and protic species, which further attack the salt: $\text{H}_2\text{O}_{\text{oxide}} + \text{PF}_5 \Rightarrow \text{PF}_3\text{O} + 2\text{HF}$, forming less fluorine coordinated salt decomposition species, observed in F1s of the charged Li₂CO₃ (Figs. S17c and 6d) and heat-treated NMC811 (Fig. 5c) to 4.2 V_{Li} and above. The atomic percent of salt decomposed product Li_xPF_yO_z and metal (oxy-)fluorides (LiM_xF_yO_z) observed for charged heat-treated NMC811 is around 20% at 4.2 V_{Li} and above (Figs. 6b and 6c), matching with the

atomic percent of salt decomposition species observed in charged as-received NMC811 in previous work,¹⁰ further suggesting the heat-treatment solely does not result in the stable salt decomposition observed in F-modified NMC811. (Fig. 6a)

F-modified NMC811 shows enhanced cycling stability compared to as-received NMC811 and heat-treated NMC811.—The reduced interfacial reactivity of F-modified NMC811 results in

improved cycling performance compared to as-received NMC811 and heat-treated NMC811. (Fig. 7) The initial discharge capacity of F-modified NMC811 is around 170 mAh g^{-1} when cycled between $4.4 V_{\text{Li}}$ and $2 V_{\text{Li}}$ at a rate of 1 C rate (280 mA g^{-1}), slightly lower compared to that of nonmodified NMC811, potentially due to removal excess Li on the oxide surface due to heat-treatment and introduction of fluorine. Upon cycling F-modified NMC811 to $4.4 V_{\text{Li}}$ in a half-cell configuration with a 1 C rate (280 mA g^{-1}), achieving a capacity retention of 94% after 100 cycles, in comparison with less than 70% capacity retention of as-received NMC811. This improvement is also manifested in the slow internal resistance buildup throughout the cycling of the F-modified NMC811, with less than 100 Ohm internal resistance upon charging to 50 cycles, in comparison with more than 150 Ohm of internal resistance of as-received NMC811 after 50 cycles. (Fig. S21) However, the internal resistance development rate of the F-modified NMC811 starts to catch up with that of as-received NMC811 after 50 cycles, indicative of potential F removal on the surface and/or the overwhelming effect of Li negative electrodes in the half-cell configuration. This change of internal resistance growth rate build-up is also evident in the cycling profile, where F-modified NMC811 starts to show a drastic increase of degradation rate after 50 cycles, which is comparable to that of the as-received NMC811.

The greater cycling stability of F-modified NMC811 is less evident when compared to that of heat-treated NMC811. The heat-treated NMC811, cycled in the same condition with the F-modified NMC811, shows slightly worse cycling performance in the first 50 cycles, but still much improved performance compared to as-received NMC811 samples. After 50th cycles, the degradation rate of F-modified NMC811 and the heat treated NMC811 is quite similar. This similar degradation might come from impact of the lithium negative electrodes and/or the cross talk between positive and negative electrodes, and to separate the impact from Li negative electrodes, further study and evaluation on full-cell performance of F-modified are needed.

Conclusions

In this work, we have shown a fluorine modification of NMC811 positive with enhanced cycling stability. Upon fluorine doping, we are able to decrease the energetic driving force of carbonate dehydrogenation on the oxide surface. Such reduced solvent decomposition is further supported by in situ IR and ex situ XPS measurement C1s and O1s spectra on the charged fluorine modified NMC811. This diminished solvent decomposition is coupled with stable salt decomposition layer deposited on the oxide layer, shown by XPS F1s spectra. By comparing the IR spectra with the heat-treated NMC811 and Li_2CO_3 composite electrodes, we are able to decouple the formation of VC and dehydrogenated EC, where oxides trigger the formation of VC in the solution phase, and metal carbonate impurities trigger the formation of dehydrogenated EC. In this work, we highlight the importance of anion engineering in controlling the cycling stability of high-energy positive electrodes. Moreover we emphasize the importance of Ni-rich NMC washing and pre-treatment to eliminate potential surface contamination and capacity degradation upon cycling.

Experimental Methods

Oxide synthesis and electrode preparation.—F-modified NMC811 is synthesized by mixing stoichiometric amount of NH_4F and $\text{LiOH} \cdot \text{H}_2\text{O}$ with the pristine NMC811 (EcoPro, South Korea) inside the glovebox in mortar and pestle for 1 h. The mixture is then heated in an oxygen flow at 600°C for 4 h with a heating and cooling rate of 2°C min^{-1} . The heat-treated NMC811 is processed by heating the pristine NMC811 (EcoPro, South Korea) in an oxygen flow at 600°C for 4 h with a heating and cooling rate of 2°C min^{-1} . By introducing 1%–5% fluorine source, 5% of fluorine substitution resulted in the most improved cycling stability after 100

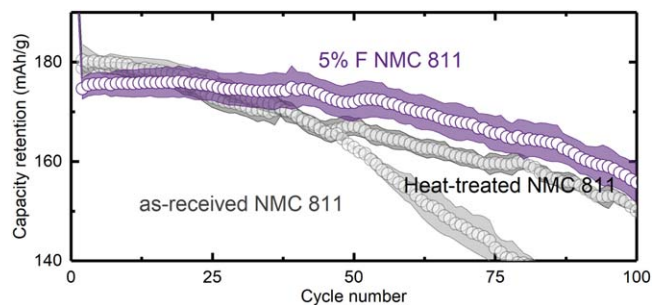


Figure 7. Capacity retention of 5% F-modified NMC811, heat-treated NMC811, and as-received NMC811 cycled between $4.4 V_{\text{Li}}$ and $2 V_{\text{Li}}$ with a current rate of 280 mA g^{-1} (1 C) and a constant current constant voltage (CCCV) cut-off upon charging with a threshold current of $C/20$ (14 mA g^{-1}), where F-modified NMC811 (with 5% nominal stoichiometric F) shows improved capacity retention in comparison with heat-treated NMC811 and NMC811, yet after 50 cycles, there is decay in all those three materials with comparable rate, potentially due to the impact from negative electrodes. The electrodes loading is around $2\text{--}3 \text{ mg cm}^{-2}$. The cycling data is reproduced with two coin cells with comparable loading, and the shaded area indicate the standard deviation of those two cells.

cycles (Fig. S22), therefore in the study we primarily present the 5% F-modified NMC811 result.

In this study, we employed oxide-only electrodes since using composite electrodes hinders extraction of useful information on solvent decomposition products in C1s (due to conductive carbon) and salt decomposition products in F1s (due to binder) in XPS. By using oxide-only electrodes, we can directly correlate the surface decomposition products and interfacial reactivity with the oxide electronic structure without the interference of carbon and binder. The carbon-free binder free electrodes were prepared by mixing active materials with N-methyl-2-pyrrolidone (NMP) (Sigma Aldrich) in a 1:100 mass ratio. After bath-sonication for 30 min, the ink was deposited on $\frac{1}{2}$ inch diameter aluminum discs and dried at 100°C . The Composite electrodes were prepared by mixing active material (85%), carbon black (2% Csp, Timcal, 5% KS6) and polyvinylidene fluoride (PVDF) (8%, Kynar) dispersed in NMP with homogenizer. The slurry was then bladed onto aluminum sheet with a gap of $10 \mu\text{m}$. Both the composite or carbon-free binder-free electrodes were punched and pressed at 6.3 T cm^{-2} under a hydraulic press, to favor embedding of the powder in the aluminum disc in the case of the carbon-free, binder-free electrodes. The resulted loading of the positive electrode materials is around $2\text{--}3 \text{ mg cm}^{-2}$. Finally, the electrodes were completely dried at 120°C under vacuum for 24 h. For the XPS characterization of Li_2CO_3 , we add in 10%wt acetylene black (AB) when making the electrodes due to the non-conductive nature of Li_2CO_3 .

The composite electrode for in situ FT-IR was composed of NMC (85 wt%, from EcoPro and Umicore) as the active material, carbon black (5 wt% KS6 and 2 wt% Super P, both from Timcal) as an electrically conductive carbon, and poly(vinylidene fluoride) (8 wt%, PVDF, Kynar) as the binder. These materials were mixed thoroughly with N-methylpyrrolidone (NMP, Aldrich) in a 1:15 mass ratio, using a planetary centrifugal mixer (THINKY AR-100). The obtained slurry was drop-casted onto glassy fiber substrates (Whatman 934-AH, 10 mm in diameter) and dried at 100°C . Then the composite composites were compressed at 0.5 T cm^{-2} using a hydraulic press to improve electrical conductivity. Finally the electrodes were completely dried at 120°C under vacuum for 24 h. The active material loading was $\sim 6.5 \text{ mg cm}^{-2}$, but it is noted here that the effective loading is smaller because some particles could permeate into the glassy fiber and not all of the loading is on the top surface.

Electrochemistry.—Electrochemical behavior of the electrodes was confirmed by galvanostatic measurements in two-electrodes

cells (Tomcell type TJ-AC). Cells were assembled in an argon-filled glovebox (<0.5 ppm of H₂O and O₂) and comprised a lithium metal foil as the negative electrode and the positive electrode, separated by two pieces of polypropylene separator (2500 Celgard), impregnated with 100 μ l of different electrolytes including LP57 (1 M LiPF₆ in a 3:7 ethylene carbonate (EC): ethylmethyl carbonate (EMC) electrolyte (BASF)). After assembly, the cells rested for 6 h prior to measurement and then were charged with different end-of-charge potentials (4.1, 4.2, 4.4, and 4.6 V_{Li}) at a C/100 rate, based on the theoretical capacity calculated assuming full delithiation. The cells were maintained at end-of-charge potential for 5 h before disassembly in the glovebox. For carbon-free binder-free electrode, the electrodes were gently rinsed with 100 μ l of EMC and dried under vacuum at room temperature for 3 h.

The composite electrodes are cycled with two formation cycles with a constant C rate of C/10 (28 mA g⁻¹) from 2 V_{Li} to 4.4 V_{Li}. The charging was conducted in a constant current constant voltage (CCCV) mode with a current cutoff of C/20 (14 mA g⁻¹) at upper cutoff potential. The cycling was conducted with a constant C rate of 1 C (280 mA g⁻¹) from 2 V_{Li} to 4.4 V_{Li}, with a CCCV cutoff of C/20 (14 mA g⁻¹) at 4.4 V_{Li} cutoff.

FT-IR spectroscopy.—An in situ FT-IR spectro-electrochemical cell is based on the design based on our previous work.¹² A calcium fluoride (CaF₂) hemisphere (Diameter 20 mm, Pier optics) was used as the optical prism, with Pt as the current collector (sputtered at $\sim 0.3 \text{ \AA s}^{-1}$ for 15 nm, as measured by an electrochemical quartz crystal microbalance), and the prism was attached to a Teflon part as the wall. The cell was assembled in an argon-filled glovebox ([H₂O] and [O₂] < 0.5 ppm, MBraun). Comprised composite NMC/glassy fiber is the positive electrode, and a lithium metal foil is the negative electrode, separated by two pieces of polypropylene separator (2325 Celgard) with 100 μ l of electrolytes. The lithium foil was covered by a stainless steel plate as a spacer, and a spring was compressed by a cap on top to reduce composite electrode electronic resistance. In this setup, NMC on the glassy fiber was placed downward and faced towards the prism, so that the IR signals could collect the surface information on NMC particles. Electrolytes could permeate through the glassy fiber, so that the diffusion is not restricted.

After assembly, the cell was first rested for 6 h. Next, galvanostatic charge were performed using BCS-COM (Biologic) and VMP3 (Biologic). Electrochemical behavior of the electrodes in the in situ FT-IR spectro-electrochemical cell was confirmed by galvanostatic measurements above. For the measurements without oxides, sputtered Pt was the positive electrode and linear sweep voltammetry was performed.

At the same time during charging or linear voltage sweeping, in situ FT-IR measurements were performed on a Tensor II (Bruker) FT-IR equipped with deuterated triglycine sulfate (DTGS) detector inside an argon-filled glovebox. The FT-IR spectra were acquired in the single-reflection mode using an attenuated total reflection (ATR) accessory (Pike Vee-Max II, Pike Technologies) at an incident angle of 50 degrees. The spectral resolution was 4 cm⁻¹ and the scan velocity was 1.6 kHz. Each spectrum was measured by superimposing 32 interferograms. All spectra were presented in the form of absorbance according to $\log(I_0/I_1)$, where I_0 and I_1 are the spectrum of background (blank Pt surface without electrolytes) and in situ spectrum of the sample, respectively.

For ex situ measurements on pristine electrolytes, the spectra were acquired in the ATR mode using a germanium (Ge) prism (Pier optics) at an incident angle of 50 degrees. Spectral settings were the same as in situ measurements. Although we assign the observed species based on DFT and solution ATR spectra, other species such as semicarbonates cannot be excluded, because there could be other features in the convoluted bands.

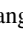
XPS measurements.—All carbon-free, binder-free electrodes were transferred from glovebox to XPS chamber using a transfer vessel (ULVAC-PHI, INC.). For each potential, at least two

electrodes were charged for reproducibility. All the XPS spectra were collected using a PHI 5000 VersaProbe II (ULVAC-PHI, INC.) using a monochromatized Al K α source and a charge neutralizer. A pass energy of 23.5 eV was used and adventitious carbon at 285 eV (C1s spectra) was used for calibration of all XPS spectra. After subtraction of a Shirley-type background, photoemission lines were fitted using combined Gaussian-Lorentzian functions, except in the case of the Co, Ni and Mn 2p_{3/2} lines where asymmetric line shapes were used. The RSF (relative sensitivity factors) values for C1s, O1s, F1s, P2p, and Li1s photoemission lines were given as 0.314, 0.733, 1, 0.525, and 0.028 respectively. The chemical compositions, binding energies and full width at half maximum of all spectra can be found in Tables S1–S3.

DFT calculations.—Periodic plane wave Density Functional Theory (DFT) calculations were performed to study the hydrogen adsorption and ligand vacancy formation energy on a number of oxides, fluorides, sulfites and phosphate surfaces. We used the PBE functional as implemented in the Vienna *Ab Initio* Simulation Package (VASP) code, and Projector Augmented Wave (PAW) for the description of the core-electron interaction, and the plane wave cutoff was set to 450 eV. The surfaces were modeled with slabs of thicknesses between 10 and 12 \AA , separated by at least 13 \AA and a dipole correction was applied in order to eliminate spurious interactions across the periodic boundary along the direction perpendicular to the surface. For the calculations to compare the hydrogen adsorption energy of F-doped LiNiO₂ and the undoped case (Fig. S1), we applied a U_{eff} = 6.4 eV on Ni, as GGA is known to delocalize the electrons and generally has inaccurate description for redox energetics for later transition metal oxides.⁴³

ORCID

Yang Yu  <https://orcid.org/0000-0001-9937-2338>

Yirui Zhang  <https://orcid.org/0000-0001-7604-8623>

Yang Shao-Horn  <https://orcid.org/0000-0001-8714-2121>

References

1. R. Jung, M. Metzger, F. Maglia, C. Stinner, and H. A. Gasteiger, "Oxygen release and its effect on the cycling stability of LiNi_xMnyCo_zO₂ (NMC) cathode materials for Li-ion batteries." *J. Electrochem. Soc.*, **164**, A1361 (2017).
2. R. Jung, M. Metzger, F. Maglia, C. Stinner, and H. A. Gasteiger, "Chemical versus electrochemical electrolyte oxidation on NMC111, NMC622, NMC811, LNMO, and conductive carbon." *The Journal of Physical Chemistry Letters*, **8**, 4820 (2017).
3. H.-J. Noh, S. Youn, C. S. Yoon, and Y.-K. Sun, "Comparison of the structural and electrochemical properties of layered Li [Ni_xCo_yMn_z] O₂ (X = 1/3, 0.5, 0.6, 0.7, 0.8 and 0.85) cathode material for lithium-ion batteries." *J. Power Sources*, **233**, 121 (2013).
4. S. Hwang, S. Y. Kim, K. Y. Chung, E. A. Stach, S. M. Kim, and W. Chang, "Determination of the mechanism and extent of surface degradation in ni-based cathode materials after repeated electrochemical cycling." *APL Mater.*, **4**, 096105 (2016).
5. Y.-K. Sun, S.-T. Myung, B.-C. Park, J. Prakash, I. Belharouak, and K. Amine, "High-energy cathode material for long-life and safe lithium batteries." *Nat. Mater.*, **8**, 320 (2009).
6. S. Hwang, S. M. Kim, S.-M. Bak, S. Y. Kim, B.-W. Cho, K. Y. Chung, J. Y. Lee, E. A. Stach, and W. Chang, "Using real-time electron microscopy to explore the effects of transition-metal composition on the local thermal stability in charged Li x Ni y Mn z Co1-y-z O2 cathode materials." *Chem. Mater.*, **27**, 3927 (2015).
7. S.-M. Bak, E. Hu, Y. Zhou, X. Yu, S. D. Senanayake, S.-J. Cho, K.-B. Kim, K. Y. Chung, X.-Q. Yang, and K.-W. Nam, "Structural changes and thermal stability of charged LiNi x Mn y Co z O2 cathode materials studied by combined in Situ time-resolved XRD and mass spectroscopy." *ACS Appl. Mater. Interfaces*, **6**, 22594 (2014).
8. D. Xiong, L. Ellis, J. Li, H. Li, T. Hynes, J. Allen, J. Xia, D. Hall, I. Hill, and J. Dahn, "Measuring oxygen release from delithiated LiNi_xMnyCo_{1-x-y}O₂ and its effects on the performance of high voltage li-ion cells." *J. Electrochem. Soc.*, **164**, A3025 (2017).
9. L. Giordano et al., "Ligand-dependent energetics for dehydrogenation: implications in li-ion battery electrolyte stability and selective oxidation catalysis of hydrogen-containing molecules." *Chem. Mater.*, **31**, 5464 (2019).
10. Y. Yu, P. Karayalali, Y. Katayama, L. Giordano, M. Gauthier, F. Maglia, R. Jung, I. Lund, and Y. Shao-Horn, "Coupled LiPF₆ decomposition and carbonate dehydrogenation enhanced by highly covalent metal oxides in high-energy li-ion batteries." *The Journal of Physical Chemistry C*, **122**, 27368 (2018).

11. L. Giordano, P. Karayaylali, Y. Yu, Y. Katayama, F. Maglia, S. Lux, and Y. Shao-Horn, "Chemical reactivity descriptor for the oxide-electrolyte interface in li-ion batteries." *The Journal of physical chemistry letters*, **8**, 3881 (2017).
12. Y. Zhang, Y. Katayama, R. Tataru, L. Giordano, Y. Yu, D. Fraggedakis, J. G. Sun, F. Maglia, R. Jung, and M. Z. Bazant, "Revealing electrolyte oxidation via carbonate dehydrogenation on Ni-based oxides in Li-Ion Batteries by in Situ fourier transform infrared spectroscopy." *Energy Environ. Sci.*, **13**, 183 (2020).
13. Z. Chen and J. Dahn, "Improving the capacity retention of LiCoO₂ cycled to 4.5 V by heat-treatment." *Electrochemical and Solid State Letters*, **7**, A11 (2003).
14. P. Karayaylali, R. Tataru, Y. Zhang, K.-L. Chan, Y. Yu, L. Giordano, F. Maglia, R. Jung, I. Lund, and Y. Shao-Horn, "Coating-dependent electrode-electrolyte interface for ni-rich positive electrodes in Li-Ion batteries." *J. Electrochem. Soc.*, **166**, A1022 (2019).
15. M. R. Laskar, D. H. Jackson, Y. Guan, S. Xu, S. Fang, M. Dreibelbis, M. K. Mahanthappa, D. Morgan, R. J. Hamers, and T. F. Kuech, "Atomic layer deposition of Al₂O₃-Ga₂O₃ alloy coatings for Li [Ni_{0.5}Mn_{0.3}Co_{0.2}] O₂ cathode to improve rate performance in Li-Ion battery." *ACS Appl. Mater. Interfaces*, **8**, 10572 (2016).
16. L. David et al., "Unveiling the role of Al₂O₃ in preventing surface reconstruction during high-voltage cycling of lithium-ion batteries." *ACS Appl. Energy Mater.*, **2**, 1308 (2019).
17. Y. Su, S. Cui, Z. Zhuo, W. Yang, X. Wang, and F. Pan, "Enhancing the high-voltage cycling performance of LiNi_{0.5}Mn_{0.3}Co_{0.2}O₂ by retarding its interfacial reaction with an electrolyte by atomic-layer-deposited Al₂O₃." *ACS Appl. Mater. Interfaces*, **7**, 25105 (2015).
18. M. J. Herzog, D. Esken, and J. Janek, "Improved cycling performance of high-nickel NMC by dry powder coating with nanostructured fumed Al₂O₃." *TiO₂ and ZrO₂: A Comparison. Batteries & Supercaps*, **4**, 1003 (2021).
19. J. O. Binder, S. P. Culver, R. Pinedo, D. A. Weber, M. S. Friedrich, K. I. Gries, K. Volz, W. G. Zeier, and J. Janek, "Investigation of fluorine and nitrogen as anionic dopants in nickel-rich cathode materials for lithium-ion batteries." *ACS Appl. Mater. Interfaces*, **10**, 44452 (2018).
20. X. Xiong, Z. Wang, X. Yin, H. Guo, and X. Li, "A modified lif coating process to enhance the electrochemical performance characteristics of LiNi_{0.8}Co_{0.1}Mn_{0.1}O₂ cathode materials." *Mater. Lett.*, **110**, 4 (2013).
21. A. T. Freiberg, J. Sicklinger, S. Solchenbach, and H. A. Gasteiger, "Li₂CO₃ Decomposition in Li-Ion batteries induced by the electrochemical oxidation of the electrolyte and of electrolyte impurities." *Electrochim. Acta*, **346**, 136271 (2020).
22. T. M. Østergaard, L. Giordano, I. E. Castelli, F. Maglia, B. K. Antonopoulos, Y. Shao-Horn, and J. Rossmeisl, "Oxidation of ethylene carbonate on li metal oxide surfaces." *The Journal of Physical Chemistry C*, **122**, 10442 (2018).
23. A. T. Freiberg, M. K. Roos, J. Wandt, R. de Vivie-Riedle, and H. A. Gasteiger, "Singlet oxygen reactivity with carbonate solvents used for li-ion battery electrolytes." *The Journal of Physical Chemistry A*, **122**, 8828 (2018).
24. J. Wandt, A. T. Freiberg, A. Ogrodnik, and H. A. Gasteiger, "Singlet oxygen evolution from layered transition metal oxide cathode materials and its implications for lithium-ion batteries." *Mater. Today*, **21**, 825 (2018).
25. U. Breddemann et al., "Fluorination of Ni-Rich lithium-ion battery cathode materials by fluorine gas: chemistry, characterization, and electrochemical performance in full-cells." *Batteries & Supercaps*, **4**, 632 (2020).
26. J. Matthew, "Surface analysis by auger and X-ray photoelectron spectroscopy.", ed. D. Briggs and J. T. Grant *IMPublications* (SurfaceSpectra, Manchester, UK) p. 900 (2003), ISBN 1-901019-04-7, 900 pp.
27. J. Matthew, *Surface and Interface Analysis*, **36**, 1647 (2004).
28. H. Ago, T. Kugler, F. Cacialli, W. R. Salaneck, M. S. Shaffer, A. H. Windle, and R. H. Friend, "Work functions and surface functional groups of multiwall carbon nanotubes." *J. Phys. Chem. B*, **103**, 8116 (1999).
29. C. Kozłowski and P. M. Sherwood, "X-Ray photoelectron-spectroscopic studies of carbon-fibre surfaces. Part 5.—The effect of PH on surface oxidation." *J. Chem. Soc., Faraday Trans. 1 F*, **81**, 2745 (1985).
30. A. T. Appapillai, A. N. Mansour, J. Cho, and Y. Shao-Horn, "Microstructure of LiCoO₂ with and without 'AlPO₄' nanoparticle coating: combined STEM and XPS studies." *Chem. Mater.*, **19**, 5748 (2007).
31. S. Verdier, E. Ouatani, L. Dedryvère, R. Bonhomme, F. Biensan, P. Gonbeau, and D. XPS, "Study on Al₂O₃-and AlPO₄-Coated LiCoO₂ cathode material for high-capacity Li ion batteries." *J. Electrochem. Soc.*, **154**, A1088 (2007).
32. S. Malmgren, K. Ciosek, M. Hahlén, T. Gustafsson, M. Gorgoi, H. A. Rensmo, and K. Edström, "Comparing anode and cathode electrode/electrolyte interface composition and morphology using soft and hard X-ray photoelectron spectroscopy." *Electrochim. Acta*, **97**, 23 (2013).
33. J.-C. Dupin, D. Gonbeau, H. Benklilou-Moudden, P. Vinatier, and A. Levasseur, "XPS analysis of new lithium cobalt oxide thin-films before and after lithium deintercalation." *Thin Solid Films*, **384**, 23 (2001).
34. K. Edström, T. Gustafsson, and J. Thomas, "The cathode-electrolyte interface in a Li-Ion battery." *Lithium-ion Batteries: Solid-Electrolyte Interphase* (Singapore) (World Scientific) p 337 (2004).
35. H. Bryngelsson, M. Sjömdahl, T. Gustafsson, and K. Edström, "How dynamic is the SEI ?" *J. Power Sources*, **174**, 970 (2007).
36. S. E. Renfrew, L. A. Kaufman, and B. D. McCloskey, "Altering surface contaminants and defects influences the first-cycle outgassing and irreversible transformations of LiNi_{0.6}Mn_{0.2}Co_{0.2}O₂." *ACS Appl. Mater. Interfaces*, **11**, 34913 (2019).
37. N. Mahne, S. E. Renfrew, B. D. McCloskey, and S. A. Freunberger, "Electrochemical oxidation of lithium carbonate generates singlet oxygen." *Angew. Chem. Int. Ed.*, **57**, 5529 (2018).
38. S. E. Renfrew and B. D. McCloskey, "Residual lithium carbonate predominantly accounts for first cycle CO₂ and CO Outgassing of Li-stoichiometric and li-rich layered transition-metal oxides." *JACS*, **139**, 17853 (2017).
39. S. E. Renfrew and B. D. McCloskey, "Quantification of surface oxygen depletion and solid carbonate evolution on the first cycle of LiNi_{0.6}Mn_{0.2}Co_{0.2}O₂ Electrodes." *ACS Appl. Energy Mater.*, **2**, 3762 (2019).
40. R. Dedryvère, H. Martinez, S. Leroy, D. Lemordant, F. Bonhomme, P. Biensan, and D. Gonbeau, "Surface film formation on electrodes in a LiCoO₂/graphite cell: a step by step XPS study." *J. Power Sources*, **174**, 462 (2007).
41. Y.-C. Lu, A. N. Mansour, N. Yabuuchi, and Y. Shao-Horn, "Probing the origin of enhanced stability of 'AlPO₄' nanoparticle coated LiCoO₂ during cycling to high voltages: combined XRD and XPS studies." *Chem. Mater.*, **21**, 4408 (2009).
42. A. Guéguen, D. Streich, M. He, M. Mendez, F. F. Chesneau, P. Novák, and E. J. Berg, "Decomposition of LiPF₆ in high energy lithium-ion batteries studied with online electrochemical mass spectrometry." *J. Electrochem. Soc.*, **163**, A1095 (2016).
43. L. Wang, T. Maxisch, and G. Ceder, "Oxidation energies of transition metal oxides within the GGA + U framework." *Physical Review B*, **73**, 195107 (2006).
44. J.-C. Dupin, D. Gonbeau, P. Vinatier, and A. Levasseur, "Systematic XPS studies of metal oxides, hydroxides and peroxides." *Phys. Chem. Chem. Phys.*, **2**, 1319 (2000).